*J. Fluid Mech.* (1973), *vol.* 59, *part* 1, *pp.* 77–95
*Printed in Great Britain*



# Numerical experiments on time-dependent rotational Couette flow

By D. C. S. LIU
TRW Systems Group, Redondo Beach, California

AND C. F. CHEN
Department of Mechanical and Aerospace Engineering,
Rutgers University, New Brunswick, N.J.

(Received 18 October 1971 and in revised form 31 October 1972)

The flow induced by impulsively starting the inner cylinder in a Couette flow apparatus is investigated by using a nonlinear analysis. Explicit finite-difference approximations are used to solve the Navier–Stokes equations for axisymmetric flows. Random small perturbations are distributed initially and periodic boundary conditions are applied in the axial direction over a length which, in general, is chosen to be the critical wavelength observed experimentally. Simultaneous occurrence of Taylor vortices is obtained at supercritical Reynolds numbers. The development of streamlines, perturbation velocity components and the kinetic energy of the perturbations is examined in detail. Many salient features of the physical flow are observed in the numerical experiments.

## 1. Introduction

The stability of time-independent flow has been the subject of intensive study. Linear stability analysis has succeeded to a remarkable degree, and the results show that the small perturbations initially present are selectively amplified when the value of a suitable parameter such as the Reynolds number exceeds a certain limit. The critical value of the parameter, as well as the wavenumber of the perturbation which first grows, have been confirmed by well-planned experimental investigations.

For time-dependent flows, the situation is quite different. The experiments are usually more difficult to perform, and the theoretical analysis is hindered by the fact that there is no suitable definition of stability. The principle of exchange of stabilities so often applied in the time-independent flows, which reduces the linear stability equation to an eigenvalue problem, is no longer applicable in time-dependent flows. This is because the perturbation are growing (or decaying) in a basic flow field which is itself evolving in time. If one is certain that the growth of the perturbations, once started, will be much faster than the evolution of the basic flow, then a quasi-steady approach can be used. With this approach, the instantaneous velocity profile is analysed for stability. However, one is never sure *a priori* of the applicability of this method since the history of the flow is not considered. Another approach to the stability problem is to treat it as an

initial-value problem in which the time evolution of the initial small random perturbations of a given wavelength is monitored by numerical integration. The growth or decay of the perturbation kinetic energy would indicate whether the flow is unstable or stable.

Recently, Chen & Kirchner (1971) investigated the stability problem of time-dependent rotational Couette flow by two different approaches. The first is the treatment as an initial-value problem and the second is the quasi-steady approach. The results show that the initial-value problem approach predicts critical wavelengths remarkably close to those found experimentally, and when the perturbation kinetic energy has increased a thousandfold, the secondary flow pattern becomes clearly observable. The quasi-steady approach has been shown to be quite inadequate to predict both the critical wavelength and the onset time, which is defined as the time when the secondary flow is first observed.

With the advent of large digital computers, numerical experiments on the evolution of the secondary flow in a steady Couette flow have been performed by several investigators. Meyer (1967) used the time-dependent numerical technique to solve the Navier–Stokes equations for steady rotational Couette flow with a radius ratio $\eta$ (of inner to outer cylinder radius) of $\frac{5}{6}$. The results for the critical Reynolds number for the onset of Taylor vortices were in good agreement with linear theory. He later extended the method to study the development of three-dimensional wavy vortex modes from either a basic laminar flow or a basic Taylor cell flow (Meyer 1969). Strawbridge & Hooper (1968) gave numerical solutions of the Navier–Stokes equations for axisymmetric flows, of which the Taylor vortex flow between infinite concentric cylinders was one of the examples. For a radius ratio of $\frac{1}{2}$, they numerically determined the streamlines of the flow. On comparison with the known observed flow pattern, good qualitative agreement was obtained. The torque acting on the cylinder was also evaluated for Reynolds numbers less than 100 with good agreement with observed values. In the present study the calculations are extended to the case of a time-dependent basic Couette flow.

In order to obtain detailed information on the development of the secondary flow in a time-dependent rotational Couette flow, we have solved numerically the nonlinear equations governing the axisymmetric motion of a fluid confined within a concentric annulus infinite in axial extent. Calculations have been made for the growth of Taylor vortices as evidenced by the deflexions of streamlines, the perturbation velocity and of the kinetic energy of perturbations. The torques acting on the inner and the outer cylinders have been calculated for one particular case in order to assess errors which may have been introduced during the numerical calculations.

## 2. Basic equations

Consider a cylindrical co-ordinate system $(r, \theta, z)$ in which the $z$ axis is aligned with the axis of concentric cylinders with radii $R_1$ and $R_2$, $R_2 > R_1$. Starting with the unsteady Navier–Stokes equations governing the axisymmetric motion within the annulus, eliminating the pressure terms, and writing the resulting

equations in terms of the perturbation vorticity $\zeta$ and the circulation function $V$, we obtain (Strawbridge & Hooper 1968)

$$\zeta_t + u\zeta_r + w\zeta_z - \frac{1}{r^4}(V^2)_z = \frac{1}{Re}\left(\zeta_{rr} + \frac{3}{r}\zeta_r + \zeta_{zz}\right), \tag{1}$$

$$V_t + uV_r + wV_z = \frac{1}{Re}\left(V_{rr} - \frac{1}{r}V_r + V_{zz}\right). \tag{2}$$

The vorticity $\zeta$ is defined as

$$\zeta = r^{-1}(u_z - w_r) \tag{3}$$

and the circulation function $V = rv$. The subscripts denote partial differentiation. The radial, circumferential and axial components of the velocity are denoted by $(u, v, w)$ and time by $t$. All quantities are dimensionless, the basic length being the radius $R_1$, of the inner cylinder, basic velocity the surface speed $R_1\Omega_1$ of the inner cylinder and basic time $\Omega^{-1}$. It is noted that, in the presentation of results, the time is reported in terms of $\tau$, which is a dimensionless time normalized with respect to the diffusion time $R_1^2/\nu$. This is to conform with our earlier work. The Reynolds number $Re$ is defined in terms of the radius and the surface speed of the inner cylinder, $Re = R_1^2\Omega_1/\nu$, where $\nu$ is the kinematic viscosity of the fluid. It is convenient to introduce the stream function $\psi$ in terms of the velocity components:

$$\psi_z = ru, \quad \psi_r = -rw. \tag{4}$$

The vorticity now becomes

$$r^2\zeta = \psi_{zz} - r^{-1}\psi_r + \psi_{rr}. \tag{5}$$

Equations (1) and (2) describe the evolution of vorticity and circulation function in time and (5) relates the vorticity to the stream function. The former two equations are parabolic and the last one is elliptic.

The no-slip boundary condition is assumed at all solid walls, whether they are stationary or moving with constant velocity, hence

$$u(1, z, t) = w(1, z, t) = 0, \quad V(1, z, t) = 1;$$

$$u(\eta^{-1}, z, t) = w(\eta^{-1}, z, t) = V(\eta^{-1}, z, t) = 0;$$

and

$$\psi(1, z, t) = \psi_r(1, z, t) = \psi_z(1, z, t) = 0;$$

$$\psi(\eta^{-1}, z, t) = \psi_r(\eta^{-1}, z, t) = \psi_z(\eta^{-1}, z, t) = 0.$$

The vorticity $\zeta$ at the boundaries is calculated from (5), hence at the solid boundaries we have

$$\zeta(1, z, t) = \psi_{rr}(1, z, t),$$

and

$$\eta^{-2}\zeta(\eta^{-1}, z, t) = \psi_{rr}(\eta^{-1}, z, t).$$

The initial condition is $V(1, z, 0) = 1$.

The infinite concentric cylinders are not totally enclosed by solid boundaries. The length $L$ of the region chosen to be investigated is still arbitrary. Owing to the periodic occurrence of the Taylor vortices observed experimentally we have chosen an axial length $L$ which is the average of the critical lengths observed by Kirchner & Chen (1970) and Liu (1971). Periodic boundary conditions are applied

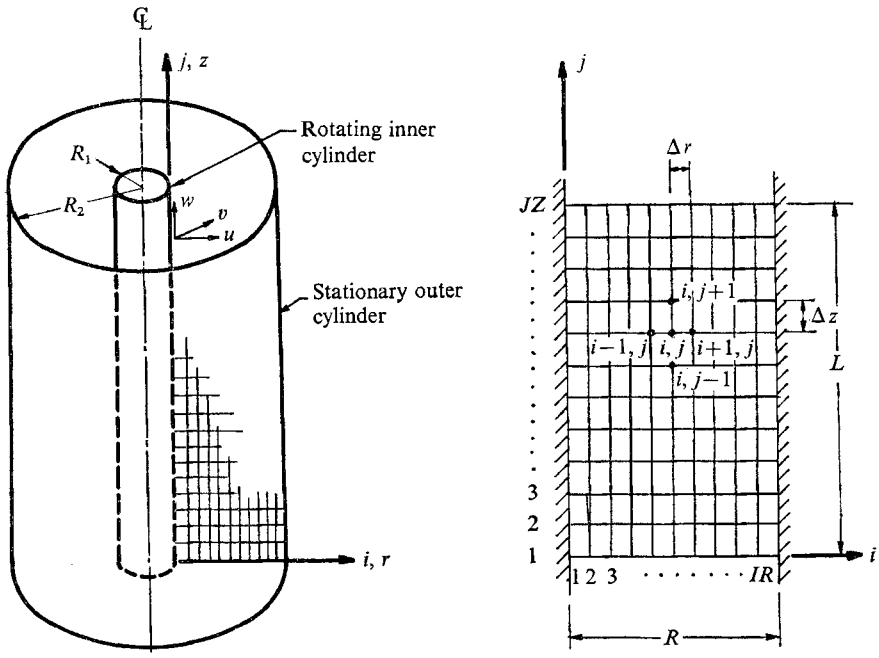


FIGURE 1. The configuration and the grid system.

with period $L$; it is required that all variables as well as their derivatives be periodic in $L$.

The perturbation kinetic energy $E_p$, per wavelength, is defined as follows:

$$E_p = \pi\rho \int_0^L \int_1^{\eta^{-1}} r(u^2+v^2+w^2)\, dr\, dz, \tag{6}$$

and the torque per wavelength is defined as

$$\Gamma|_r = 2\pi r^2 L\mu r(v/r)_r, \tag{7}$$

where $\rho$ is the density and $\mu$ is the dynamic viscosity of the fluid.

## 3. Difference equations and computational procedure

A rectangular grid system is constructed on the axial plane of the field of flow as shown in figure 1. The derivatives of the equations developed in the previous section are approximated by finite differences, and then solved at discrete intervals of space and time. It is convenient to characterize the variables $r, z$ and $t$ by $i, j$ and $k$, that is

$$\begin{aligned} r &= 1+(i-1)\Delta r \quad (i = 1,2,3,\ldots), \\ z &= (j-1)\Delta z \quad (j = 1,2,3,\ldots), \\ t &= k\Delta t \quad (k = 1,2,3,\ldots). \end{aligned}$$

Here, $\Delta r$ and $\Delta z$ are the spatial increments in the radial and axial directions, respectively, and $\Delta t$ is the time increment.

Central-difference approximation is used for spatial derivatives and forward-difference approximation is used for time derivatives. The finite-difference forms of (1) and (2) are quite similar. Let $Q$ be a general variable. The value of $Q$ at the grid point $(i,j)$ and $(k+1)$th time step is

$$Q_{i,j}^{k+1} = Q_{i,j} + \Delta t \left\{ \frac{1}{Re} \left[ \frac{Q_{i+1,j} + Q_{i-1,j} - 2Q_{i,j}}{(\Delta r)^2} + \frac{Q_{i,j+1} + Q_{i,j-1} - 2Q_{i,j}}{(\Delta z)^2} + A \frac{Q_{i+1,j} - Q_{i-1,j}}{2r_i(\Delta r)} \right] + B \frac{1}{r_i^4} V_{i,j} \frac{V_{i,j+1} - V_{i,j-1}}{\Delta z} - u_{i,j}(Q_r)_{i,j} - w_{i,j}(Q_z)_{i,j} \right\}, \tag{8}$$

where

$$A = \begin{cases} 3, \\ -1, \end{cases} \qquad B = \begin{cases} 1 & \text{for } Q = \zeta, \\ 0 & \text{for } Q = V. \end{cases}$$

For the elliptic equation (5), the method of successive iteration with an over-relaxation factor $\theta$ is used. The $(n+1)$th iterate is (Todd 1962, p. 392)

$$\psi_{i,j}^{n+1} = \psi_{i,j}^{n}(1-\theta) + \theta \left\{ \frac{1}{2[(\Delta r)^2 + (\Delta z)^2]} \left[ \left(1 - \frac{\Delta r}{2r_i}\right)(\Delta z)^2 \psi_{i+1,j}^{n} + (1 + \Delta r/2r_i)(\Delta z)^2 \psi_{i-1,j}^{n+1} + (\Delta r)^2 (\psi_{i,j+1}^{n} + \psi_{i,j-1}^{n+1}) - r_i^2 (\Delta r \Delta z)^2 \zeta_{i,j} \right] \right\}. \tag{9}$$

A finite-difference equation is said to be stable and convergent if its solution remains bounded and converges to the solution of the corresponding differential equation as time approaches infinity and the spatial and time increments per calculation cycle tend to zero. In both cases, the specific criterion is that, in the space or time interval, the magnitude of the change in any field variable must be small compared with the magnitude of the variable itself. However, decreases in mesh spacing require not only much more computer storage, but they also require decreases in the time interval per calculation cycle. Lax's equivalence theorem (Richtmyer & Morton 1967, p. 45) states that, for a given properly posed initial-value problem and a finite-difference approximation to it that satisfies the consistency condition, stability is the necessary and sufficient condition for convergence. That is, the stability implies convergence if the truncation error associated with the difference equation tends to zero as the spatial and time increments tend to zero. Using the method of stability analysis as suggested by Richtmyer & Morton (1967), the following criteria must be met:

$$\frac{\Delta t}{Re} \left\{ \frac{2}{(\Delta r)^2} + \frac{2}{(\Delta z)^2} + \frac{\|u\| Re}{\Delta r} + \frac{\|w\| Re}{\Delta z} \right\} \leqslant 1. \tag{10}$$

where $\|u\|$ = maximum value of $|u_{i,j}|$

and $\|w\|$ = maximum value of $|w_{i,j}|$.

In the calculations the left-hand side of equation (10) is equated to 0·5.

The convective terms $u(\partial Q/\partial r)$ and $w(\partial Q/\partial z)$ in the governing equations are

evaluated by using a forward or a backward space difference according to whether $u, w < 0$ or $u, w > 0$. From Taylor series expansion,

$$u_{i,j}\left(\frac{\partial Q}{\partial r}\right)_{i,j} = \begin{Bmatrix} u_{i,j}\dfrac{Q_{i,j}-Q_{i-1,j}}{\Delta_r} \\ u_{i,j}\dfrac{Q_{i+1,j}-Q_{i,j}}{\Delta_r} \end{Bmatrix} + |u|\frac{\Delta r}{2}\frac{\partial^2 Q}{\partial r^2} + o(\Delta r)^2 \quad \begin{matrix} u_{i,j} \geqslant 0, \\ u_{i,j} < 0, \end{matrix} \tag{11a}$$

$$w_{i,j}\left(\frac{\partial Q}{\partial z}\right)_{i,j} = \begin{Bmatrix} w_{i,j}\dfrac{Q_{i,j}-Q_{i,j-1}}{\Delta z} \\ w_{i,j}\dfrac{Q_{i,j+1}-Q_{i,j}}{\Delta z} \end{Bmatrix} + |w|\frac{\Delta z}{2}\frac{\partial^2 Q}{\partial z^2} + o(\Delta z)^2 \quad \begin{matrix} w_{i,j} \geqslant 0, \\ w_{i,j} < 0. \end{matrix} \tag{11b}$$

It is seen that spurious diffusion terms have been introduced. In order to be sure that these diffusion terms have negligible contribution to final results, we must have

$$\tfrac{1}{2}Re|u|\Delta r, \tfrac{1}{2}Re|w|\Delta z \ll 1. \tag{12}$$

Torrance (1968) has shown that, if one starts with the conservation form of the governing equation and uses a first-order numerical scheme, false diffusion terms still arise. However, the final result gives better agreement with that using higher order numerical schemes. In a natural convection problem, he has shown that when non-conservation equations are used there are fictitious sources or sinks in the flow field. As a result the heat flux into the control volume is different from that out of the volume. However, the isotherms and streamlines obtained by either the conservation methods or non-conservation methods are qualitatively the same. In the subsequent calculations, the quantities in (12) are continuously monitored and the times when these quantities exceed $10^{-2}$ for all cases treated are noted. However, calculations for later times are still carried out with the belief that the resulting flow patterns are essentially correct.

The calculations are initiated by assigning small random values of vorticity of order $10^{-5}$ at each internal grid point. These initial perturbations must, of course, satisfy the periodic boundary condition. Equation (9) is then used to calculate the stream function $\psi_{i,j}$ iteratively. The iterations are terminated when the maximum relative error of two successive iterates is within the specific limit, generally taken as $10^{-4}$. From the values of $\psi_{i,j}$, $u_{i,j}$ and $w_{i,j}$ are evaluated through (4) and the boundary vortices are calculated at this time. A time step is then chosen, and the rotating inner boundary assumes its prescribed speed instantaneously. Values of $V_{i,j}$ and $\zeta_{i,j}$ are evaluated according to (8). With new values of the $\zeta_{i,j}$, the entire sequence of calculations is repeated and the solution is thus advanced in time. The kinetic energy of the perturbed flow is evaluated by Simpson's rule at each time step when flow field is calculated.

The entire procedure could have been initiated by assigning random disturbances in the stream function $\psi$. With this procedure, however, there is no assurance that the initial perturbations in the velocity and vorticity are of uniformly small order of magnitude because of the differentiation processes involved.

## 4. Results and discussion

The numerical results are presented here for impulsively started circular Couette flow with a stationary outer cylinder. All calculations were made in double precision on an IBM 360–67 computer. A total of 18 cases with different combinations of $Re$ and $\eta$ have been calculated; they are listed in table 1. Results are presented in terms of the flow field, the distribution of perturbation velocities, the growth of the perturbation kinetic energy, and the torque acting on the cylinders. These are separately discussed below.

### 4.1. *Flow field*

Results are primarily shown by streamline plots obtained by linear interpolation between grid points by the use of an IBM 1130 computer together with a Cal Comp 1627 plotter. In each figure, such as figure 2, several frames of streamline plots at different times are shown. In each frame, the vertical boundary on the left-hand side is the surface of the rotating inner cylinder and that on the right-hand side is the surface of the outer cylinder. The grid size used is shown along the inner wall and the bottom surface. The top and bottom surfaces are the periodic boundaries. Each frame consists of two wavelengths with the results repeated.

The sizes of the grids are determined by numerical experiments. It is found that with ten grid points in an axial wavelength good results of streamlines can be obtained within reasonably short computing time. The wavelengths, as was mentioned before, are adopted on the basis of the critical wavelengths observed experimentally for that particular Reynolds number.

Figure 2 (case 8) is a typical picture showing the growth of the perturbation stream function with respect to time. The Reynolds number is 300 and $\eta = \frac{1}{3}$. The first three frames show vertical streamlines, which means that the perturbation flow field consists of essentially axial velocities. These velocities, of course, are of very small magnitude. It is to be remarked that the values of the stream function are not the same for the streamlines in different frames. Their orders of magnitude are $10^{-4}$ initially and increase by one to two orders of magnitude in the eyes of the vortices at later times. The values of $\psi$ for this and subsequent streamline plots are listed in Liu (1971). At $\tau = 0{\cdot}04$, periodic radial motion can be seen at the inner boundary; the disturbances there are being amplified. At $\tau = 0{\cdot}05$, vortices can be detected along the surface of the inner cylinder. At $\tau = 0{\cdot}10$, which corresponds to 17·4 s, it is found that the region close to the outer cylinder is still not aware of the secondary motion being generated near the inner cylinder.

The effect of a vertical extent $L$ of the region other than the critical wavelength is studied first. Meyer (1967) has found that a preferred wavelength can be selected when the axial length $L$ is long enough to permit the growth of four Taylor vortices. The preferred wavelength is that which gives four equal cells. When the axial length is only long enough to permit the growth of two Taylor vortices, there is no preferred wavelength; the cells are always equal in size. In view of these results, we started our computation for $Re = 300$ and

| Case | Reynolds number $Re$ | Radius ratio $\eta$ | Region of investigation $R \times L$ | Grid point $IR \times JZ$ | $\tau$ when $\frac{1}{2}Re\|u\|\Delta r \approx 0{\cdot}01$ | Final $\tau$ reached | Computing time consumed (min) | Remarks |
|---|---|---|---|---|---|---|---|---|
| 1 | 600 | $\frac{1}{2}$ | $1 \times 4$ | $7 \times 21$ | | 0·120 | 10·7 | $IX = 1$† preliminary calculation |
| 2 | 600 | $\frac{1}{2}$ | $1 \times 0{\cdot}4$ | $11 \times 21$ | 0·025 | 0·201 | 124·1 | — |
| 3 | 600 | $\frac{1}{2}$ | $1 \times 0{\cdot}4$ | $7 \times 11$ | 0·030 | 2·240 | 21·0 | — |
| 4 | 600 | $\frac{1}{5}$ | $4 \times 0{\cdot}4$ | $21 \times 11$ | 0·035 | 0·060 | 25·2 | — |
| 4 (*a*) | 600 | $\frac{1}{5}$ | $4 \times 0{\cdot}5$ | $21 \times 11$ | 0·030 | 0·055 | 30·2 | — |
| 5 | 500 | $\frac{1}{5}$ | $4 \times 0{\cdot}45$ | $21 \times 11$ | 0·040 | 0·060 | 25·2 | — |
| 5 (*a*) | 500 | $\frac{1}{5}$ | $4 \times 0{\cdot}55$ | $21 \times 11$ | 0·035 | 0·060 | 30·2 | — |
| 6 | 400 | $\frac{1}{5}$ | $4 \times 0{\cdot}6$ | $21 \times 11$ | 0·045 | 0·100 | 30·4 | — |
| 7 | 300 | $\frac{1}{2}$ | $1 \times 0{\cdot}7$ | $7 \times 11$ | 0·060 | 0·100 | 20·1 | — |
| 8 | 300 | $\frac{1}{3}$ | $2 \times 0{\cdot}7$ | $11 \times 11$ | 0·065 | 0·100 | 16·4 | — |
| 9 | 300 | $\frac{1}{3}$ | $2 \times 0{\cdot}7$ | $11 \times 11$ | 0·060 | 0·100 | 28·0 | $IX = 999$ |
| 10 | 300 | $\frac{1}{3}$ | $2 \times 0{\cdot}56$ | $11 \times 9$ | 0·085 | 0·100 | 22·9 | $L = 0{\cdot}8Z$ |
| 11 | 300 | $\frac{1}{3}$ | $2 \times 0{\cdot}91$ | $11 \times 14$ | 0·065 | 0·100 | 22·9 | $L = 1{\cdot}3Z$ |
| 12 | 300 | $\frac{1}{3}$ | $2 \times 1{\cdot}05$ | $11 \times 16$ | 0·065 | 0·100 | 22·9 | $L = 1{\cdot}5Z$ |
| 13 | 300 | $\frac{1}{4}$ | $3 \times 0{\cdot}7$ | $16 \times 11$ | 0·065 | 0·100 | 18·1 | — |
| 14 | 300 | $\frac{1}{5}$ | $4 \times 0{\cdot}7$ | $21 \times 11$ | 0·065 | 0·100 | 23·0 | — |
| 15 | 300 | $\frac{1}{5}$ | $4 \times 0{\cdot}7$ | $21 \times 11$ | 0·065 | 0·100 | 24·4 | Half region disturbed initially‡ |
| 16 | 200 | $\frac{1}{5}$ | $4 \times 1{\cdot}0$ | $21 \times 11$ | 0·110 | 0·150 | 17·7 | — |

† $IX = 1$ is an integer to start RANDU, unless noted otherwise.
‡ Unless otherwise noted, full region disturbances were used.

TABLE 1. List of cases investigated numerically

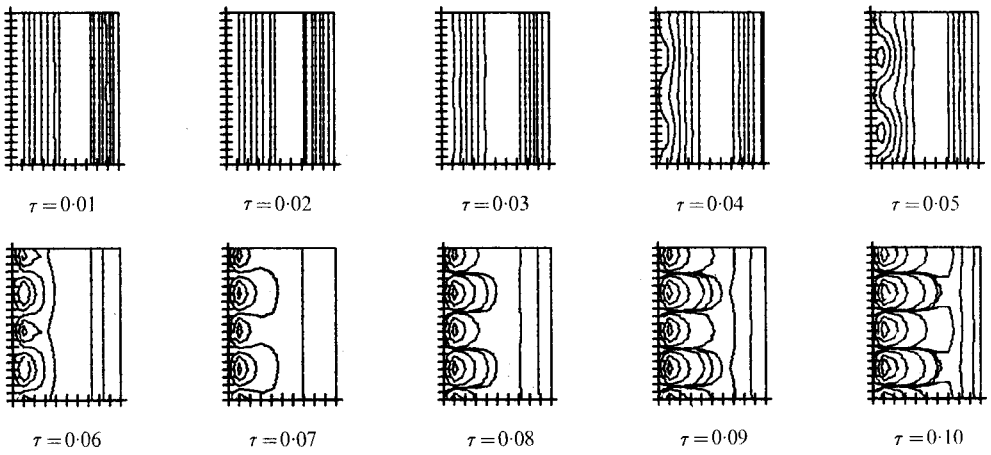


FIGURE 2. Onset of secondary flow at $Re = 300$, $R \times 2L = 2{\cdot}0 \times 1{\cdot}4$.

$\eta = \frac{1}{3}$ with $L = 2Z$, $Z$ being the average wavelength observed experimentally. Quite surprisingly, only two Taylor vortices developed. This is because our initial disturbances are completely random with periodicity imposed at the two ends. In Meyer's case, however, the disturbances were distributed along a radius at the middle of the domain considered, thus introducing a degree of symmetry into the problem. He also has shown that the initial sinusoidal conditions influence the fluid flow configuration to a considerable degree. It becomes apparent that, with our initial conditions, only two vortices can be generated. We therefore focused our attention on $L < 2Z$. It is our belief that the present set of completely random initial conditions approximates more closely to what happens in a physical experiment. The results are shown in figure 3 for $L = 0{\cdot}8Z$, $1{\cdot}2Z$ and $1{\cdot}5Z$ (cases 10, 11 and 12). It is found that, when the length assumed is less than one wavelength, the growth of the disturbances is very much delayed compared with the experimental observation. When the length assumed is equal to or greater than one wavelength, the growth of the disturbances is compatible with that observed. The point is further borne out by the kinetic energy calculations discussed later. It is interesting to note that, when the axial length equals one critical wavelength, the Taylor cells are of equal size. Meyer (1967) used this fact as a criterion for critical wavelength selection for steady Couette flows. In the present case, however, this does not offer a clear-cut selection of the critical wavelength.

With the Reynolds number kept constant at 300, the effect of different radius ratios is then examined. Streamline plots for $\eta = \frac{1}{5}$, $\frac{1}{4}$ and $\frac{1}{2}$ (cases 14, 13 and 7) are compared with result for $\eta = \frac{1}{3}$ in figure 4 at selected time intervals. It is seen that the smaller the gap the earlier the vortex pattern is established. Although the difference between $\eta = \frac{1}{5}$ and $\frac{1}{4}$ is almost negligible, the difference between $\eta = \frac{1}{5}$ and $\frac{1}{2}$ is quite noticeable. This may be attributed to the fact that, with the smaller gap, the basic velocity distribution is established earlier than in a wide-gap case. The effect of Reynolds number on the onset of secondary flow is examined by studying all 8 cases for $\eta = \frac{1}{5}$. The streamline plots show that

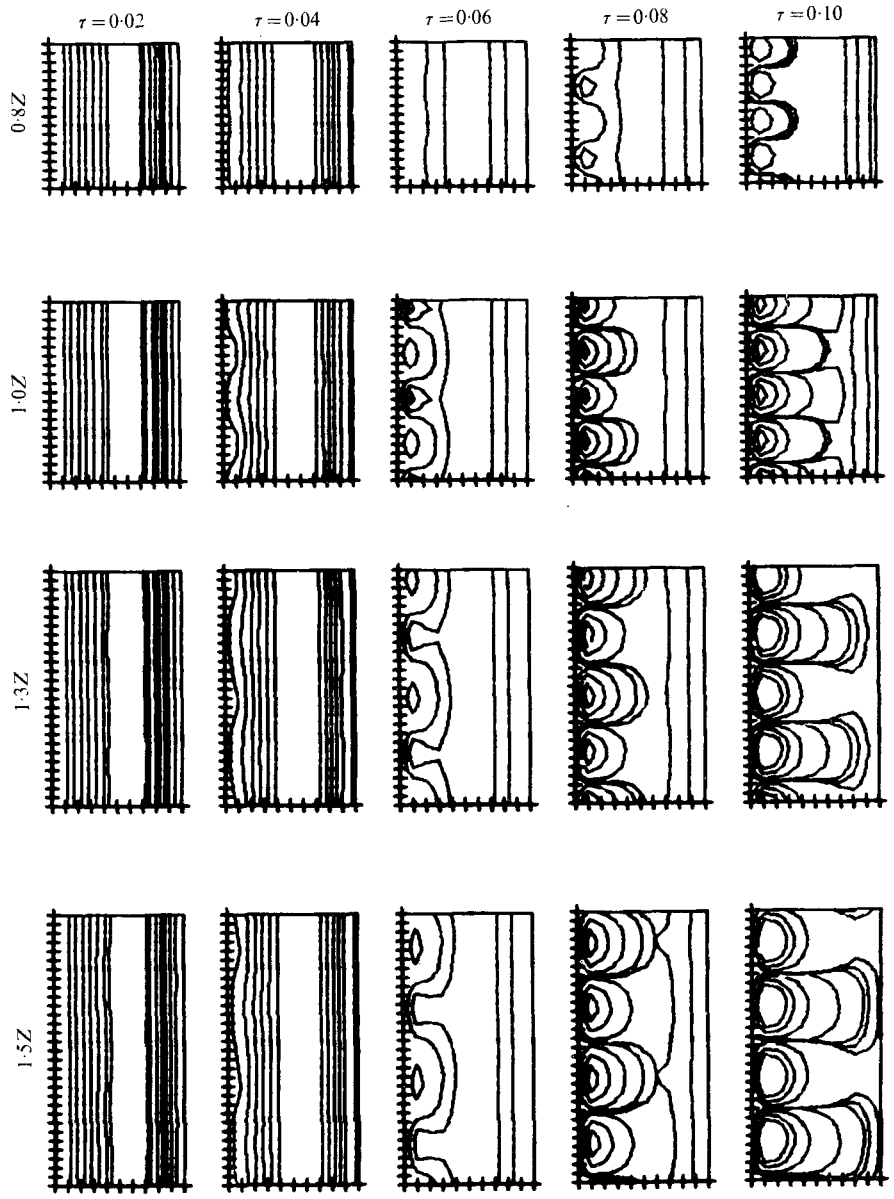


FIGURE 3. Time development of streamlines at $Re = 300$, $\eta = \frac{1}{3}$. Effect of initially assumed periodic length.

the initiation and growth of the secondary flow is similar for all Reynolds numbers. However the time of onset of the secondary flow become smaller when the Reynolds number is increased. If we define the onset time of the secondary flow as the time when the streamline near the inner cylinder exhibits periodic radial deflexions, then the agreement between the calculated and experimental values is quite good as is shown by table 2.

A remark has to be made here about the initial disturbances which are used to initiate all the calculations of the flow field. The initial random small dis-

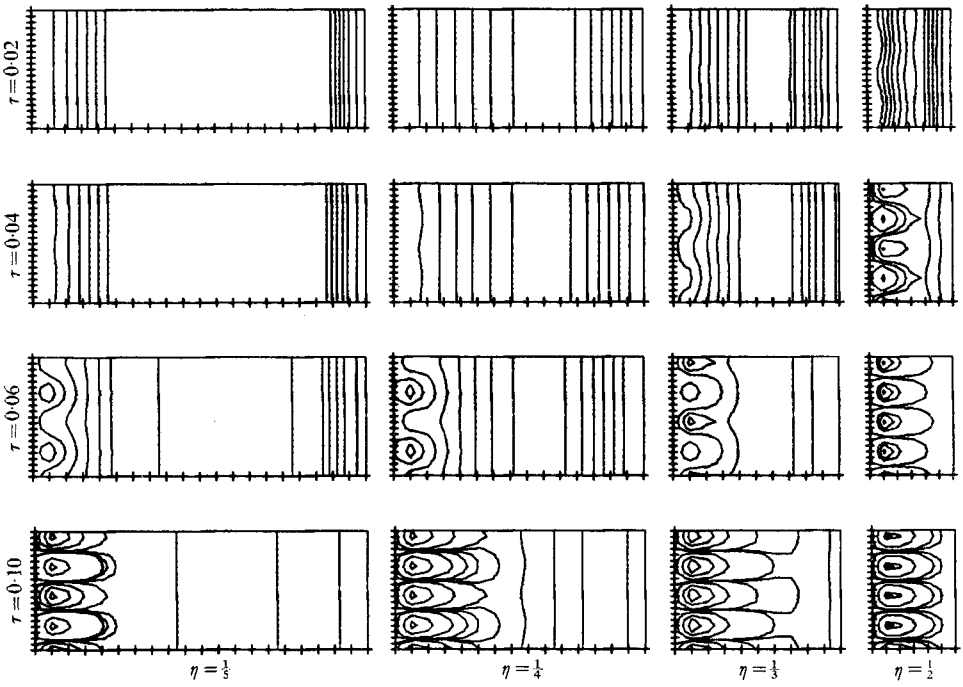


FIGURE 4. Effect of gap width on the onset of secondary flow at $Re = 300$.

| | Time of onset of secondary flow | |
|---|---|---|
| *Re* | Streamline plots | Experimental observation |
| 200 | ~ 0·080 | 0·065–0·095 |
| 300 | ~ 0·050 | 0·050–0·060 |
| 400 | ~ 0·030 | 0·032–0·040 |
| 500 | ~ 0·030 | 0·022–0·028 |
| 600 | ~ 0·025 | 0·018–0·022 |

TABLE 2

turbances in the vorticity are generated by RANDU†. An odd integer is needed to start this subroutine; two different values, 1 and 999, are tried (cases 8 and 9) for the same Reynolds number 300 and $\eta = \frac{1}{3}$. No difference can be detected from these results. The effect of the distribution of random disturbances is also studied for case 14 and case 15. The random disturbances are initially distributed throughout the entire region in case 14 whereas in case 15 the initial disturbances are confined to the left half (the inner half) of the region. Both results show a critical time around $\tau = 0{\cdot}05$ and no significant difference in streamline values after $\tau = 0{\cdot}06$. But the initial motion is more vigorous when the entire region is initially perturbed, case 14.

The effect of the magnitude of the initial disturbances on the final results has also been studied. We have varied the order of magnitude of the initial dis-

† An IBM subroutine from the IBM 360 Scientific Subroutine Package.

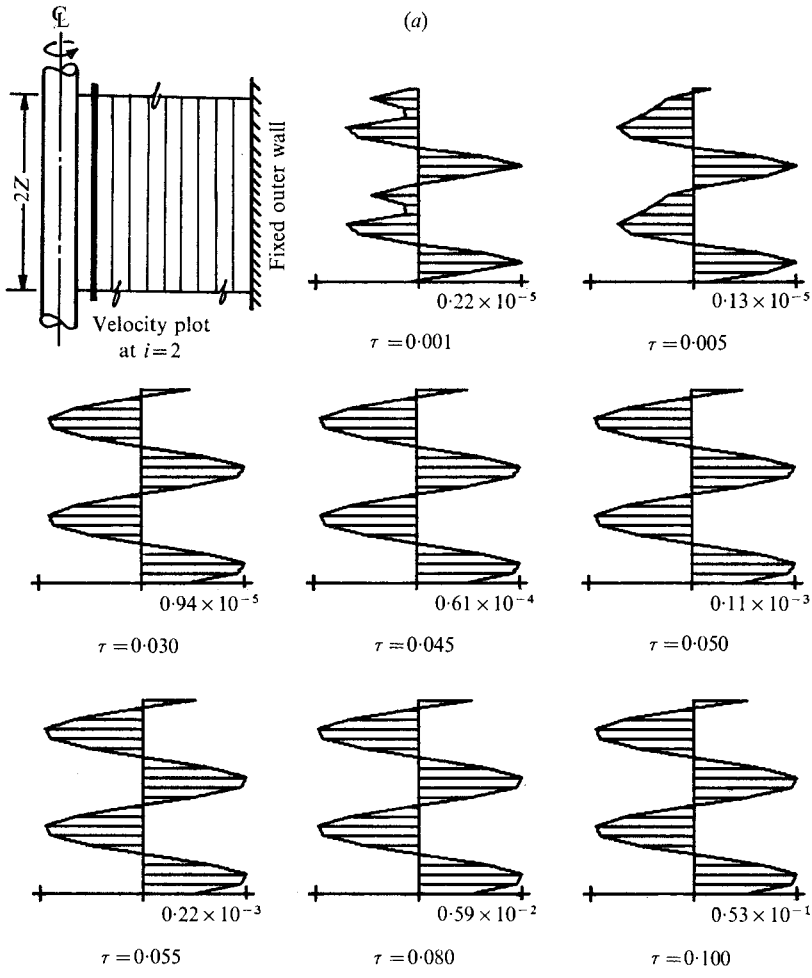


FIGURE 5. For legend see facing page.

turbances from $10^{-4}$ to $10^{-6}$. No discernible difference has been detected either in the streamline patterns or in the growth of the perturbation kinetic energy. This is not surprising since the deflexion of the streamlines is proportional to $u/w$ and the kinetic energy is normalized with respect to its initial value. For initial disturbances of magnitude $10^{-7}$ or smaller, one is taxing the capabilities of the computer. For disturbances of magnitude $10^{-3}$ or higher, one may encounter finite disturbance effects.

### 4.2. *Perturbation velocity distribution*

In order fully to characterize the flow field, the radial and axial components of the perturbation velocity at selected positions within the annulus are shown in figures 5 and 6. Figure 5 shows the radial velocity distributions and figure 6 shows the axial velocity distributions. In each figure, the graph on the upper left-hand corners shows the grid system used and the heavy line indicates the position where the velocity distribution is plotted. At each position, velocity distributions

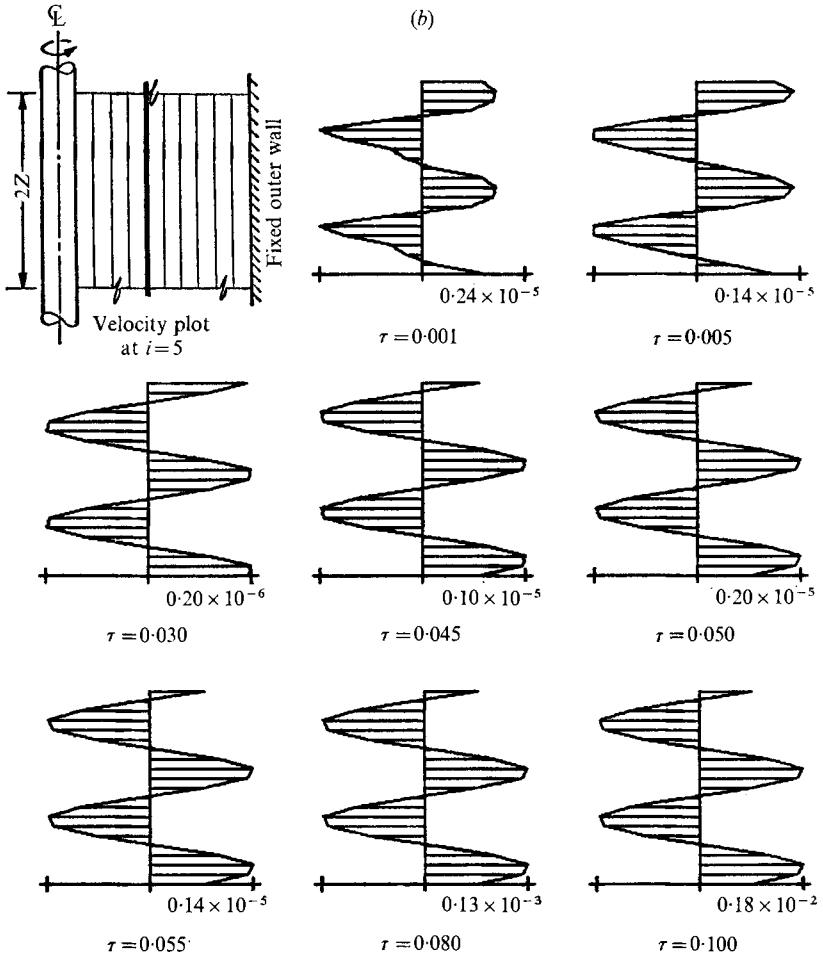


FIGURE 5. Radial perturbation velocity distribution at $Re = 300$, $\eta = \frac{1}{3}$. (*a*) $i = 2$. (*b*) $i = 5$.

at progressively later times are shown in sequence for $\tau = 0{\cdot}001$, $0{\cdot}005$, $0{\cdot}030$, $0{\cdot}045$, $0{\cdot}050$, $0{\cdot}055$, $0{\cdot}080$ and $0{\cdot}100$. At each value of $\tau$, the velocity is normalized with respect to the maximum value, which is indicated on the plot. To provide an order of magnitude of the actual velocity involved, it is noted that a non-dimensional velocity of $0{\cdot}01$ corresponds to $0{\cdot}024$ cm/s at $Re = 300$ with distilled water, and $R_1 = 1{\cdot}27$ cm. The radial perturbation velocities are presented over an axial distance of two wavelengths whereas the axial perturbation velocities are presented over one wavelength.

At $\tau = 0{\cdot}001$, the effect of the initial distribution of random perturbations still remains, as evidenced particularly by the rather jagged $u$ distribution throughout the annulus as shown in figure 5(*a*). However, by $\tau = 0{\cdot}005$, the initial randomness has been smoothed out by viscous diffusion, and the magnitude of $u$ decreases. The radial velocity next to the wall begins to grow at $\tau = 0{\cdot}030$. This growth is reflected in the slight perturbation of the essentially vertical streamlines

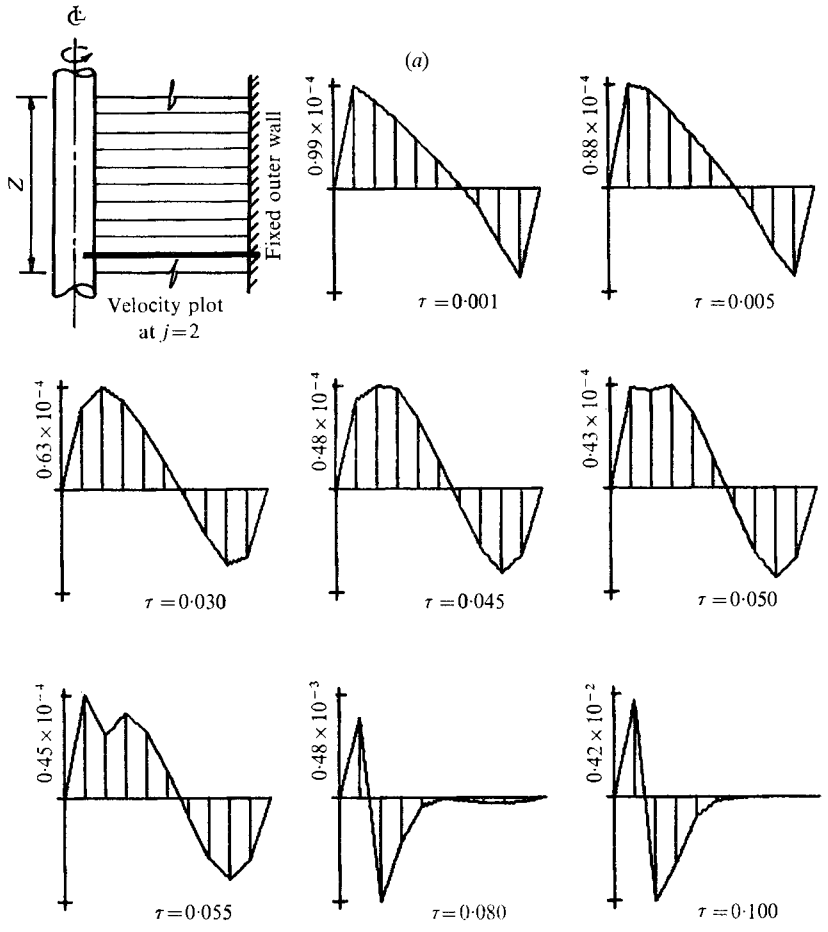


FIGURE 6. For legend see facing page.

as shown in figure 2, and by $\tau = 0{\cdot}04$, the effect of the increased radial velocity is clearly exhibited in the streamline plot. At positions successively further away from the inner cylinder, the time when the radial velocity starts to grow becomes progressively later as shown in figure 5 (*b*). At later times the $u$ component shows almost exactly a sinusoidal form. If a finite Fourier series were used to represent the $u$ distribution in two complete wavelengths, the magnitude of the odd harmonics would be much smaller than that of the even ones. This would indicate that a correct wavelength had been selected according to a criterion advanced by Meyer (1967).

The axial velocity distribution (figure 6) shows an initial up-and-down motion of the fluid. It is noted that the axial component of the velocity is about one or two orders of magnitude larger than the radial component. This is because the vertical boundaries of the inner and outer cylinders severely restrict radial motion whereas in the vertical direction, the boundary condition only insists that the velocities be the same at the top as at the bottom of the region of interest. It must be pointed out, however, that the physical magnitudes of these velocities

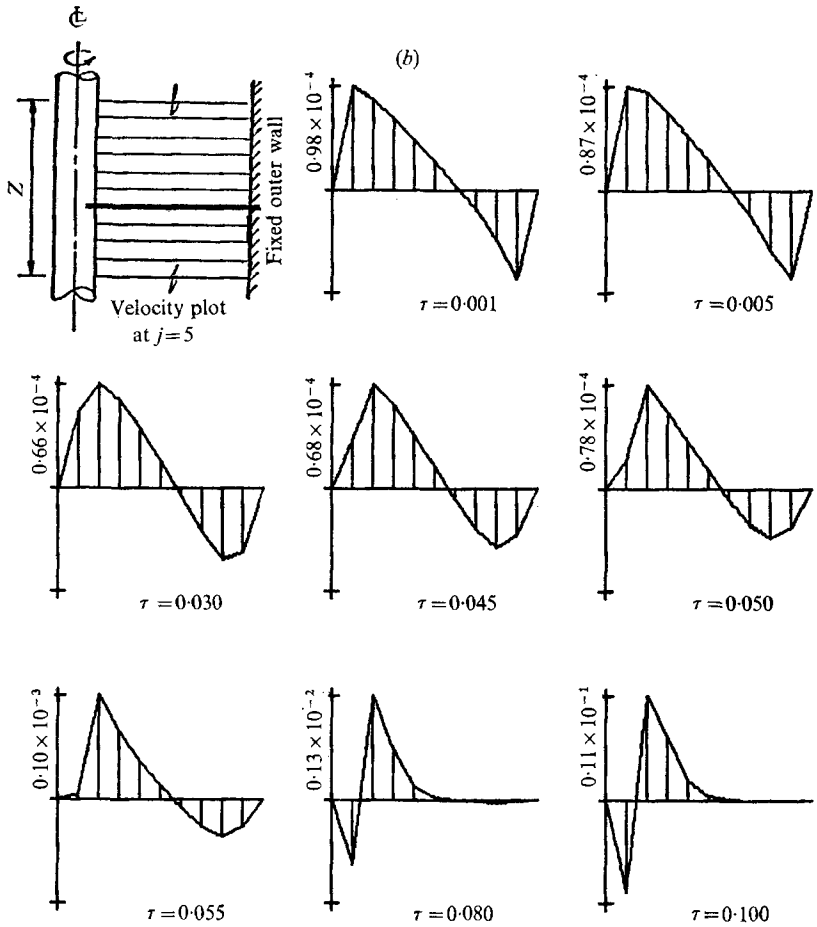


FIGURE 6. Axial perturbation velocity distribution at $Re = 300$, $\eta = \frac{1}{3}$. (*a*) $j = 2$. (*b*) $j = 5$.

are still extremely small, of the order $2{\cdot}4 \times 10^{-4}$ cm/s for the case cited. This initial vertical motion is slowly decaying owing to diffusion. At $\tau = 0{\cdot}045$, the axial velocity along a line which passes through the eye of the vortex begins to grow as shown in figure 6(*b*) (cf. figure 2 for position of $j = 5$ horizontal grid). At any position other than the centre of the vortex, the times when the axial velocities begin to grow occur later, as shown in figure 6(*a*). At $\tau = 0{\cdot}10$, all perceptible vertical motions are confined within the vortices, which extend to about 0·7 of the gap width (cf. figure 2).

### 4.3. *Kinetic energy of the perturbations*

Chen & Kirchner (1971) have computed the growth of the kinetic energy of the perturbation $E_p$ using linear stability theory. They have shown that, by examining the growth of $E_p$, the critical wavelength may be obtained. We have calculated $E_p$ for cases shown in figures 3 and 4 and the results are shown in figure 7. In figure 7(*a*), the evolution of $E_p$, normalized with respect to its initial value, is shown for $L/Z = 0{\cdot}8$, 1·0, 1·3 and 1·5 at $Re = 300$ and $\eta = \frac{1}{3}$. For all cases, the

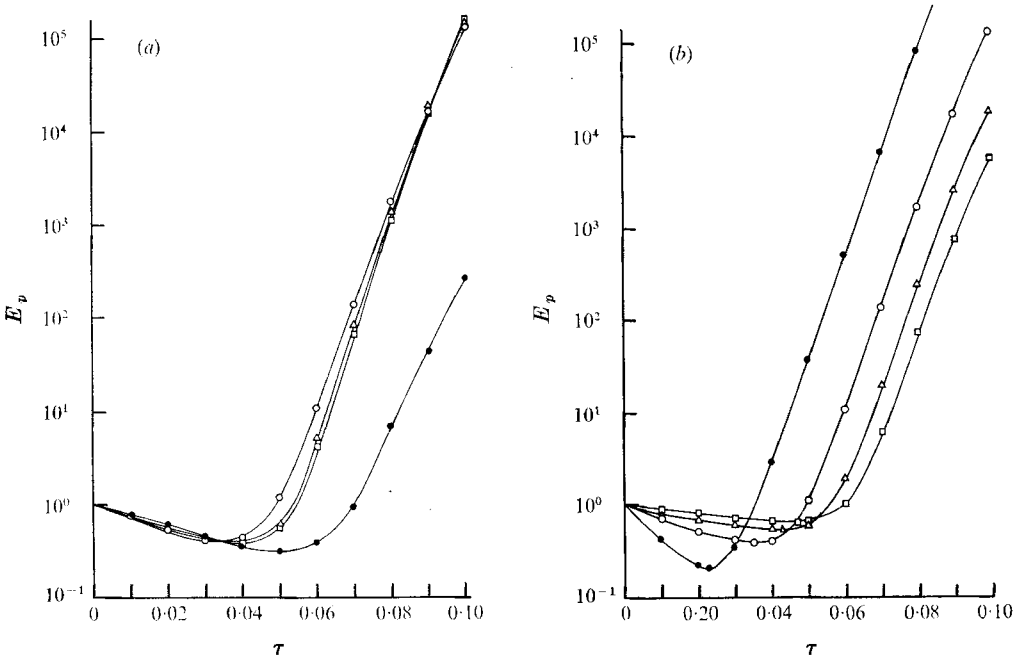


FIGURE 7. Growth of the kinetic energy of the perturbations at $Re = 300$. (*a*) Effect of initially assumed wavelength. $\eta = \frac{1}{3}$. ●, $L = 0{\cdot}8z$; ○, $L = 1{\cdot}0z$; △, $L = 1{\cdot}3z$; □, $L = 1{\cdot}5z$. (*b*) Effect of gap width. ●, $\eta = \frac{1}{2}$; ○, $\eta = \frac{1}{3}$; △, $\eta = \frac{1}{4}$; □, $\eta = \frac{1}{5}$.

perturbation kinetic energy decays initially owing to viscous damping. As energy is being fed from the basic flow, $E_p$ grows exponentially. Depending on the wavelengths initially assumed, the growth is attained at an earlier or a later time. It is seen that significant delay in reaching the minimum value is shown for $L = 0{\cdot}8Z$. For $L$ equal to or larger than one wavelength, the behaviours of the perturbation energies are similar except that the $L = 1{\cdot}0Z$ case shows a slightly faster growth rate. This result correlates well with the streamline plots shown in figure 3. We remark here that neither the energy growth nor the streamline pattern shows a clear-cut preference for a particular wavelength. This may explain the fact that, experimentally, the vortices are never quite of the same size.

The effect of varying gap width is shown in figure 7 (*b*). The gap width of the annulus is varied from 1 to 4 while the rotational speed of the inner cylinder is kept the same. The rate of growth of $E_p$ is essentially constant for all cases. The smaller gap case gives a faster rate of decay owing to the restraining effect of the side walls and an earlier start of the secondary flow. This latter fact correlates well with the stream function map as shown in figure 4. With the radius ratio kept constant at $\eta = \frac{1}{5}$, the time when the perturbation kinetic energy reaches a minimum is decreased when the Reynolds number is increased. This fact correlates well with the results obtained for the onset time by examining the streamline plots.

Since the present nonlinear calculations are initiated by distributing random perturbations of extremely small magnitude, it had been anticipated at first

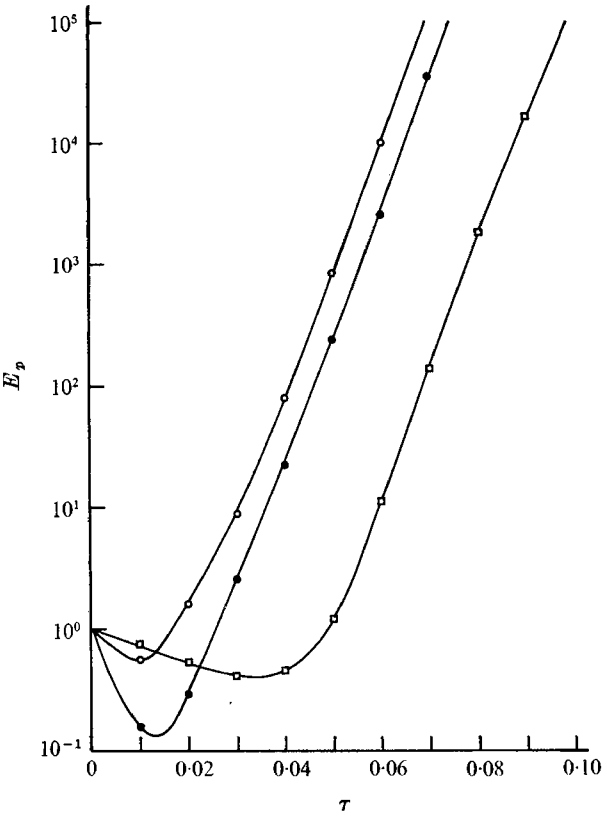


FIGURE 8. Comparison of linear and nonlinear results on the growth of the kinetic energy of the perturbations. $Re = 300$, $\eta = \frac{1}{3}$. ○, nonlinear, $\cos(2\pi z)/Z$; ●, linear; □, nonlinear, random.

that the present results would be similar to those obtained by Chen & Kirchner (1971) using the linearized theory. However, in the linear theory all disturbances are assumed to be sinusoidal whereas in the nonlinear problem they are only required to be periodic. Since the final secondary flow pattern is sinusoidal, it is then reasonable to expect that an initial disturbance which is sinusoidal would be most efficient in extracting energy from the basic flow. This is indeed the case as shown in figure 8, in which the results of linear and nonlinear calculations are compared for $Re = 300$ and $\eta = \frac{1}{3}$. It is seen that $E_p$ as calculated by the linear theory decreases much more rapidly, reaches the minimum at an earlier time, and starts exponential growth much sooner than that calculated by the nonlinear theory. The growth rates attained at later times as calculated by these two methods are essentially the same. When the initial disturbances for the nonlinear case are assumed to be $f(r)\cos 2\pi z/Z$, where $f(r)$ is a random function of $r$, the resulting $E_p$ becomes very close to that of the linear theory. The difference in the initial decay period is probably due to the differences in the exact distribution of the initial disturbances. The nonlinear calculation is probably a more realistic representation of the laboratory experiments. However, using the linearized theory, constant results can still be obtained.

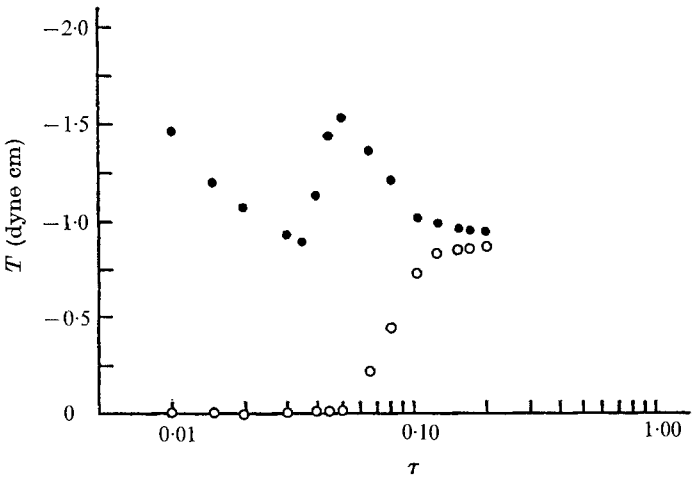


FIGURE 9. Torque $T$ on the inner and outer cylinders. $Re = 600$, $\eta = \frac{1}{2}$, $R_1 = 1{\cdot}27$ cm, $R_2 = 2{\cdot}54$ cm. ●, inner cylinder; ○, outer cylinder.

### 4.4. *Torque calculation*

In order to assess the effect of the fictitious source terms in the finite-difference scheme, we have made a calculation of the time variation of the torque acting on the surfaces of both inner and outer cylinders for $Re = 600$ and $\eta = \frac{1}{2}$. The results are shown in figure 9. The torque acting on the inner cylinder decreases initially in much the same way as for a rotating cylinder in an infinite fluid. When the presence of the outer cylinder is felt, the torque starts to increase. At this time, the torque on the outer cylinder is still negligible. When the disturbances reach the outer wall ($\tau \simeq 0{\cdot}05$), the torque on the inner cylinder is at its maximum value and is beginning to decrease whereas the torque on the outer cylinder is starting to increase rapidly. At $\tau = 0{\cdot}2$, the torques on the inner and outer cylinders are 0·948 and 0·861 dyne cm/wavelength, respectively. The 10 % discrepancy may be attributed to the spurious source terms. It is interesting to note that the experimental value of the torque obtained by Donnelly & Simon (1960) is 1·04 dyne cm/wavelength in the steady state.

## 5. Summary

In the present investigation a nonlinear mathematical model of the viscous, time-dependent, rotating Couette flow with axisymmetric motion has been formulated and solved. The system of nonlinear partial differential equations is solved by numerical techniques using the explicit finite-difference approximations. Periodic boundary conditions are imposed in the axial direction over a length which is, for most cases, the average critical wavelength observed in the experimental investigation. Small random disturbances in the vorticity are distributed initially throughout the region of interest. The time evolution of the streamline plots reveals the simultaneous occurrence of Taylor vortices all along the inner cylinder. The time of onset of the secondary flow correlates well with experimental

observations. The kinetic energy of the perturbations first decays owing to viscous damping and then grows exponentially. Owing to the initial distribution of random disturbances, the perturbations grow at the later time than the linear theory indicates. However, when a sinusoidal initial disturbance is used, the growth of the perturbation kinetic energy becomes quite similar to that of the linear theory. Spurious source terms introduced by the finite-difference approximations of the non-conservative form of the equations probably account for the 10 % difference in the torque values calculated for the inner and outer cylinders.

In conclusion, we exhibit the results of physical and numerical experiments at at $R = 300$† and $\tau = 0{\cdot}07$ in figure 10 (plate 1). The numerical calculations are for $\eta = \frac{1}{3}$ and the physical results are obtained with $\eta = \frac{1}{5}$. The left-hand borders of both the computer plot and the photograph represent the surface of the inner cylinder, which is rotating. For the computer plot, the output is repeated nine times vertically. In the physical experiment dyed fluid particles are initially evenly distributed along the inner cylinder. After the onset of the secondary flow, these particles are being swept out radially between counter-rotating vortices. These are indicated schematically in the figure. As the dye spreads out radially, they assume a disk-like shape surrounding the inner cylinder. The uneven sizes of the disks in the radial direction indicate that the secondary flow is not initiated at the same time all along the inner cylinder. Those disks which are initiated first exhibit some portions of the return flow.

This research was supported by the National Science Foundation under Grants GK-2096 and GK-14275.

## REFERENCES

CHEN, C. F. & KIRCHNER, R. P. 1971 Stability of time-dependent rotational Couette flow. Part 2. Stability analysis. *J. Fluid Mech.* **48**, 365–384.

DONNELLY, R. J. & SIMON, N. J. 1960 An empirical torque relation for supercritical flow between rotating cylinders. *J. Fluid Mech.* **7**, 401–418.

KIRCHNER, R. P. & CHEN, C. F. 1970 Stability of time-dependent rotational Couette flow. Part 1. Experimental investigation. *J. Fluid Mech.* **40**, 39–47.

LIU, D. C. S. 1971 Physical and numerical experiments of time-dependent rotational Couette flow. Ph.D. thesis. Dept. of Mechanics and Materials Science, Rutgers University.

MEYER, K. A. 1967 Time-dependent numerical study of Taylor vortex flow. *Phys. Fluids*, **10**, 1874–1879.

MEYER, K. A. 1969 Three-dimensional study of flow between concentric rotating cylinders *Phys. Fluids*, **12**, II-165–II-170.

RICHTMYER, R. D. & MORTON, K. W. 1967 *Difference Methods for Initial Value Problems*, 2nd edn. Interscience.

STRAWBRIDGE, D. R. & HOOPER, G. T. J. 1968 Numerical solutions of the Navier–Stokes equations for axisymmetric flows. *J. Mech. Engng Sci.* **10**, 389–401.

TODD, J. 1962 *Survey of Numerical Analysis.* McGraw-Hill.

TORRANCE, K. E. 1968 Comparison of finite difference computations of natural convection. *J. Res. Nat. Bur. Stand.* B **72**, 281–301.

† The physical experiment was run at $Re = 307$.

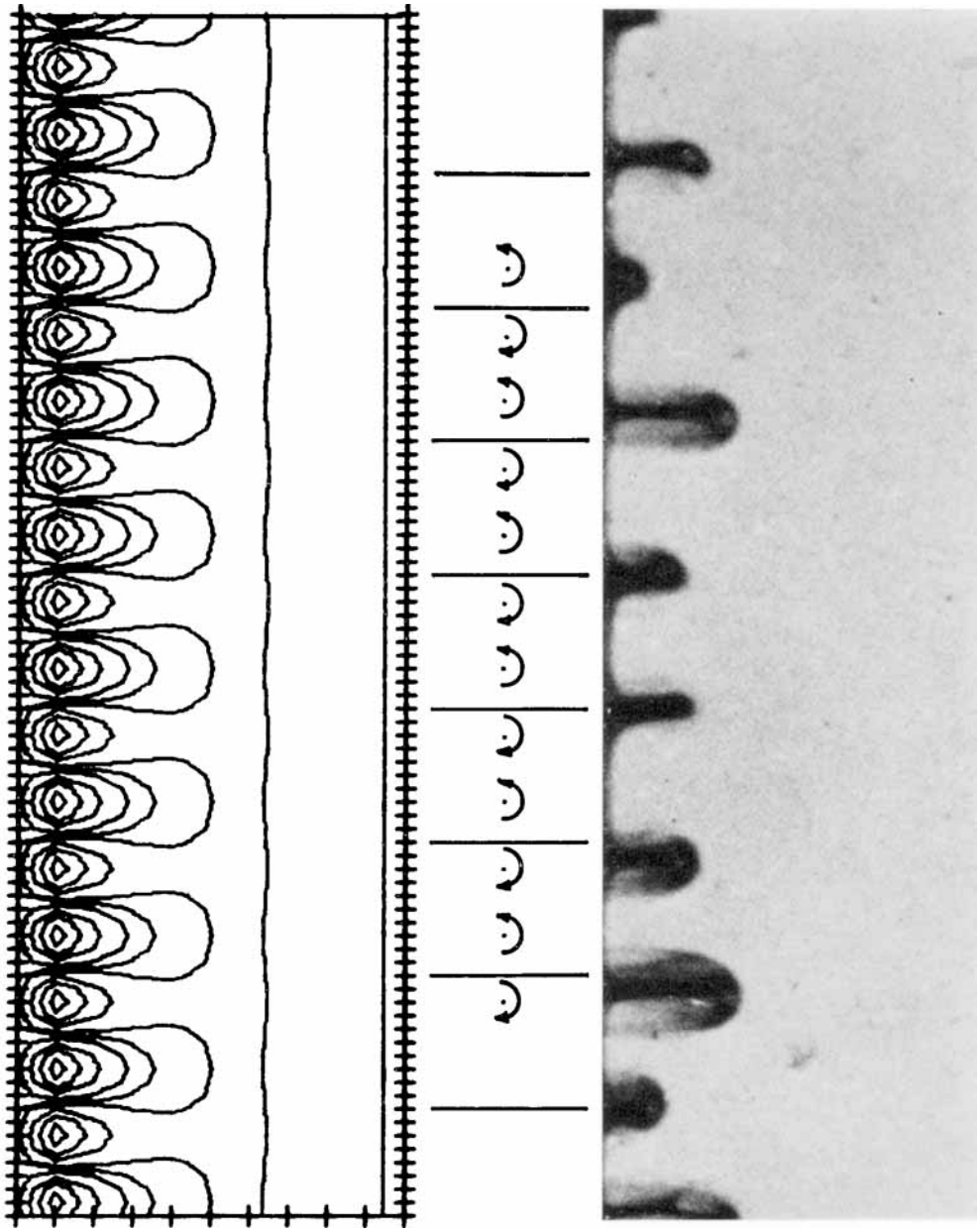

FIGURE 10. Results of the physical and numerical experiments at $Re \cong 300$.